

The Milky Way Galaxy as a Strong Gravitational Lens

E.M. Shin* and N.W. Evans*

Institute of Astronomy, University of Cambridge, Madingley Road, Cambridge, CB3 0HA, United Kingdom

9 October 2018

ABSTRACT

We study the gravitational lensing effects of spiral galaxies by taking a model of the Milky Way and computing its lensing properties. The model is composed of a spherical Hernquist bulge, a Miyamoto-Nagai disc and an isothermal halo. As a strong lens, a spiral galaxy like the Milky Way can give rise to four different imaging geometries. They are (i) three images on one side of the galaxy centre (‘disc triplets’), (ii) three images with one close to the centre (‘core triplets’), (iii) five images and (iv) seven images. Neglecting magnification bias, we show that the core triplets, disc triplets and fivefold imaging are roughly equally likely. Even though our models contain edge-on discs, their image multiplicities are not dominated by disc triplets. The halo is included for completeness, but it has a small effect on the caustic structure, the time delays and brightnesses of the images.

The Milky Way model has a maximum disc (i.e., the halo is not dynamically important in the inner parts). Strong lensing by nearly edge-on disc galaxies breaks the degeneracy between the relative contribution of the disc and halo to the overall rotation curve. If a spiral galaxy has a sub-maximum disc, then the astroid caustic shrinks dramatically in size, whilst the radial caustic shrinks more modestly. This causes changes in the relative likelihood of the image geometries, specifically (i) core triplets are now $\sim 9/2$ times more likely than disc triplets, (ii) the cross section for threefold imaging is reduced by a factor of $\sim 2/3$, whilst (iii) the cross section for fivefold imaging is reduced by $\sim 1/2$. Although multiple imaging is less likely (the cross sections are smaller), the average total magnification is greater. The time delays are smaller, as the total projected lensing mass is reduced.

Key words: gravitational lensing – Galaxy: structure – Galaxy: disc – Galaxy: bulge – Galaxy: halo

1 INTRODUCTION

In gravitational lensing, galaxies are often represented in a very idealized manner. For example, models in which either the potential or the density are stratified on similar concentric ellipses have been widely studied (Kassiola & Kovner 1993; Kormann, Schneider & Bartelmann 1994; Witt 1996; Witt & Mao 1997; Hunter & Evans 2001; Evans & Hunter 2002). Such simple, analytic models often yield valuable insights and are reasonable enough as representations of elliptical galaxies. They are less well-suited for spiral galaxies, in which the effects of the disc, bulge and halo all need to be taken into account.

Gravitational lensing by spiral galaxies has received attention from Keeton & Kochanek (1998), who studied the properties of Mestel and Kuzmin discs embedded in isothermal haloes. Wang & Turner (1997) found an analytically tractable model of a homogeneous disc embedded in an isothermal sphere, which is nonetheless realistic enough to illustrate a number of the important effects. The presence of a disc makes lensing effects sensitive to inclination. In particular, a nearly edge-on disc causes three images

to form on the same side of the lens, a configuration which has possibly been observed in APM08279+5255 (Ibata et al. 1999). Moller & Blain (1998) used ray-tracing to confirm some of the theoretical results of Keeton & Kochanek (1998).

Of the ~ 90 strong lenses, only a handful are known to be spiral galaxies (see e.g., Jackson et al. 2000; Winn et al. 2003). The most extensively studied spiral galaxy strong lens is B1600+434 (see e.g., Koopmans et al. 1998; Jackson et al. 2000). This is a two-image system, composed of a nearly edge-on lens at $z = 0.414$ lensing a background quasar at $z = 1.6$. Winn et al. (2003) studied another two-image system, PMN J2004-1349, for which the lens is an isolated spiral galaxy with an inclination angle of $\sim 70^\circ$. There are at least two known four-image lenses, Q2237+0305 (see e.g., Schmidt et al. 1998; Trott & Webster 2002) and B0712+472 (see e.g., Jackson et al. 1998; Kawano et al. 2004). Bartelmann & Loeb (1998) suggest that the underabundance of spiral lenses in optical searches may be caused by extinction by dust and that the missing lenses can be recovered in radio searches. Bartelmann (2000) makes the important point that lensing by spiral galaxies may dominate over ellipticals once angular resolutions of the order of $0.1''$ can be achieved. He showed that for the projected Next Generation

* E-mail: ems@ast.cam.ac.uk; nwe@ast.cam.ac.uk

Space Telescope, there may be of the order of 10 quasars per square degree brighter than $V \approx 26$ lensed by spirals.

Maller et al. (2000) and Winn et al. (2003) emphasise the unique contribution that studies of gravitational lensing of edge-on spirals can provide. In the Milky Way galaxy, it has been a matter of debate as to whether the disc is “maximum” or not (see e.g., Sellwood & Sanders 1988; Sackett 1997). A spiral galaxy has a maximum disc if the inner parts of its rotation are completely dominated by the disc and bulge, rather than the dark halo. Although recent evidence strongly supports the idea of a maximum disc for the Milky Way (Englmaier & Gerhard 1999; Häfner et al. 2000; Binney & Evans 2001), the relative contributions of the disc, bulge and the halo to the flat rotation curves of external spiral galaxies remains uncertain (see e.g. Courteau & Rix 1999; Palunas & Williams 2000). The issue of whether spiral galaxies typically possess a maximum disc could be resolved by the study of a sample of edge-on spirals acting as lenses, as gravitational lensing effects are sensitive to the relative masses in the rounder halo or flatter disc components. The first steps in this direction have been taken by Maller et al. (2000) who concluded that the spiral lens of B1600+434 is not maximum.

In this paper, we pick a model of the Milky Way galaxy with bulge, disc and halo that is widely-used in Galactic astronomy (see e.g., Johnston et al. 1995; Dinescu et al. 1999; Helmi 2004; Fellhauer et al. 2006) and ask what its lensing properties would be, if it were acting as a gravitational lens at a redshift of $z \approx 0.4$. The model is composed of a Hernquist (1990) bulge, Miyamoto-Nagai (1975) disc and an isothermal halo, combined so as to reproduce a flattish rotation curve of amplitude $\sim 220 \text{ kms}^{-1}$ at the Sun. This model has a maximum disc. We first discuss the lensing properties of the Hernquist bulge and Miyamoto-Nagai disc in §2 and §3, before combining them with an isothermal halo in §4 to give the full Milky Way model. We investigate how the lensing properties change as the masses of the components are varied – in particular, as the disc changes from maximum to sub-maximum.

2 THE HERNQUIST BULGE

The Hernquist (1990) model was developed for elliptical galaxies and the bulges of spiral galaxies. The three-dimensional Hernquist mass distribution is

$$\rho(\hat{r}) = \frac{M_b}{2\pi} \frac{r_0}{\hat{r}(\hat{r} + r_0)^3}, \quad (1)$$

where r_0 is a “core radius” and \hat{r} is the spherical polar radius. Integrating (1) along the line of sight yields

$$\sigma(R) = \frac{M_b}{2\pi} \frac{1}{r_0^2(1-u^2)^2} [(2+u^2)\chi(u) - 3], \quad (2)$$

where R is the radial coordinate in the lens plane and $u = R/r_0$, while

$$\chi(u) = \begin{cases} \frac{\text{sech}^{-1}u}{\sqrt{1-u^2}}, & 0 \leq u \leq 1. \\ \frac{\sec^{-1}u}{\sqrt{u^2-1}}, & u \geq 1. \end{cases} \quad (3)$$

For convenience, we follow Schneider et al. (1992) in defining the dimensionless quantities

$$r = \frac{\hat{r}}{\xi_0}, \quad \kappa(r) = \frac{\sigma(\xi_0 r)}{\sigma_{\text{cr}}}, \quad \sigma_{\text{cr}} = \frac{c^2 D_s}{4\pi G D_1 D_{1s}}, \quad (4)$$

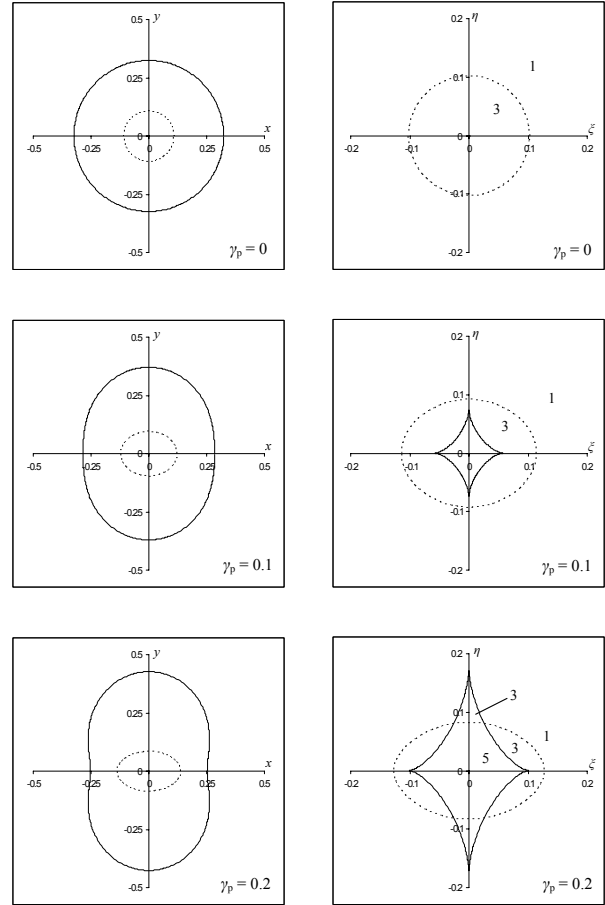


Figure 1. Critical curves (left) and caustics (right) of Hernquist lenses with different strengths of shear. The regions of multiple imaging in the source plane are labelled. In the top panels ($\gamma_p = 0$), spherical symmetry ensures that the tangential caustic is a degenerate point at the origin. In the middle panels ($\gamma_p = 0.1$), the tangential caustic (full curve) is wholly contained within the radial caustic (dotted curve). In the lower panels ($\gamma_p = 0.2$), the cusps of the tangential caustic pierce the radial caustic (so called “naked cusps”).

with D_s , D_l , D_{1s} being the distances to the source, lens, and between lens and source, and ξ_0 an arbitrary scale length. Now, the bending angle for a circularly symmetric lens is

$$\alpha(r) = \frac{2}{r} \int_0^r r' \kappa(r') r' dr' = \frac{m(r)}{r}. \quad (5)$$

Integrating (2) and choosing the scaling $\xi_0 = r_0$ gives us the bending angle of the Hernquist model as

$$\alpha(r) = m_b \frac{r}{1-r^2} (\chi(r) - 1), \quad m_b = \frac{M_b}{\pi \sigma_{\text{cr}} r_0^2}. \quad (6)$$

Introducing $\bar{\kappa}(r) = m(r)/r^2$, then the lens equation including any quadrupole perturbation is

$$\begin{pmatrix} \xi \\ \eta \end{pmatrix} = [1 - \bar{\kappa}(r)] \begin{pmatrix} x \\ y \end{pmatrix} - \begin{pmatrix} \Gamma_1 & 0 \\ 0 & \Gamma_2 \end{pmatrix} \begin{pmatrix} x \\ y \end{pmatrix}, \quad (7)$$

where (x, y) are dimensionless (length scale ξ_0) Cartesian coordinates in the lens plane and (ξ, η) are dimensionless coordinates in the source plane (length scale $\eta_0 = \xi_0 D_s/D_l$). The components $\Gamma_{1,2}$ are given by $\kappa_p \pm \gamma_p$, where κ_p is the density of a uniform sheet of matter superimposed on the lens and γ_p is the shear.

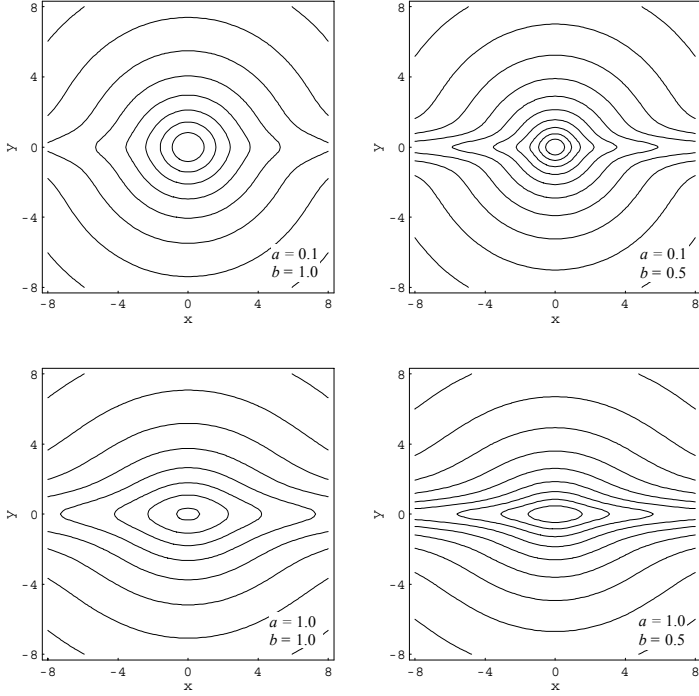


Figure 2. Level curves of the logarithm of the convergence ($\log_{10} \kappa$) for the Miyamoto-Nagai disc with $m_d = 1.0$. Contours are at intervals of 0.5. The projected density can be dimpled (upper panels) or highly flattened (lower panels).

Direct differentiation yields the components of the Jacobian matrix $A_{ij} = \frac{\partial \xi_i}{\partial x_j}$, from which we obtain the image magnification $\mu = 1/\det A$,

$$\begin{aligned} A_{11} &= 1 - \bar{\kappa}(r) - \Gamma_1 - \frac{x^2}{r} \bar{\kappa}'(r), \\ A_{12} &= A_{21} = -\frac{xy}{r} \bar{\kappa}'(r), \\ A_{22} &= 1 - \bar{\kappa}(r) - \Gamma_2 - \frac{y^2}{r} \bar{\kappa}'(r). \end{aligned} \quad (8)$$

The critical curves are given by $\mu^{-1} \equiv \det A = 0$, i.e.

$$(1 - \bar{\kappa} - \Gamma_1)(1 - \bar{\kappa} - \Gamma_2) - (1 - \bar{\kappa} - \Gamma_1) \frac{y^2}{r} \bar{\kappa}' - (1 - \bar{\kappa} - \Gamma_2) \frac{x^2}{r} \bar{\kappa}' = 0. \quad (9)$$

Neither the critical curves nor the image positions can be found analytically, but both can be found numerically. The critical curves and caustics are plotted in Figure 1 for different γ_p for $m_h = 1$, $\kappa_p = 0$; the numbers of images of sources in different regions of the source plane are shown. Varying m_h and κ_p changes the sizes of the critical curves and caustics but not their asymmetry. The number of images is odd, not even. The three-dimensional mass-density is singular at $\hat{r} = 0$ and the surface density is logarithmically divergent at $r = 0$, but the bending angle α and the deflection potential are continuous and finite, so the odd-number theorem applies. This is consistent with the study of Evans & Wilkinson (1998) on cusped density distributions and image numbers. They found that that cusps less severe than isothermal ($\kappa \propto r^{-1}$) give rise to an odd number of images, but those more severe than isothermal give rise to an even number of images.

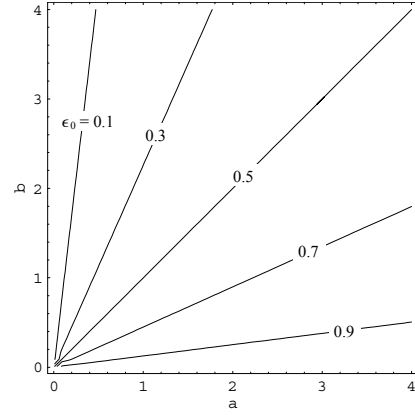


Figure 3. The central ellipticity of the projected mass distribution of the Miyamoto-Nagai disc is constant along lines of constant gradient in (a, b) parameter space. Along such lines, models closer to the origin are ‘diskier’ (possess a stronger ridge along the x -axis).

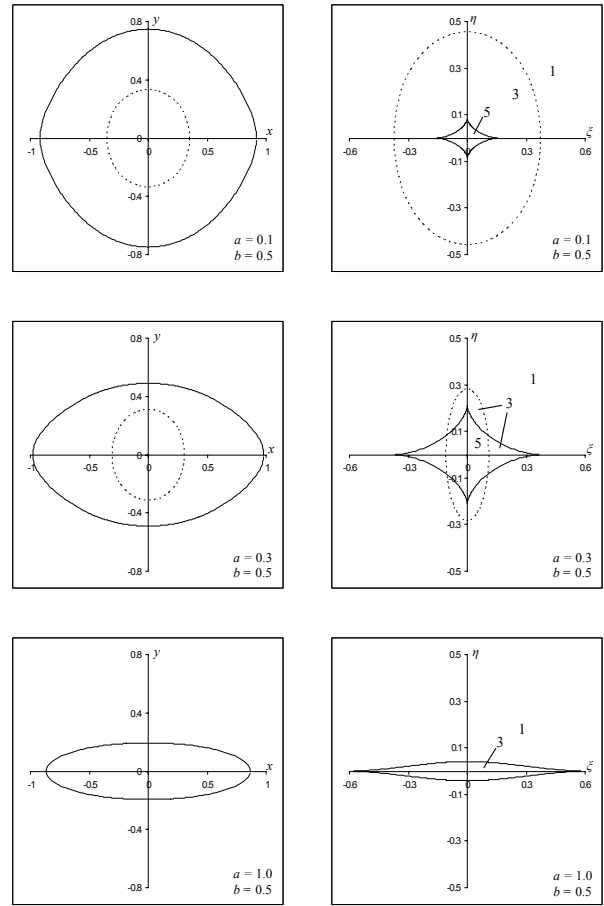


Figure 4. Critical curves (left) and caustics (right) for the Miyamoto-Nagai disc with $m_d = 1.0$ and various values of a and b . The central ellipticity of the projected density contours is 0.16 (upper panels), 0.37 (middle) and 0.67 (lower). The regions of multiple imaging in the source plane are labelled. Note that the disc model contains the same mass, but that the central surface density is diminishing on moving from the top panels to the bottom panels.

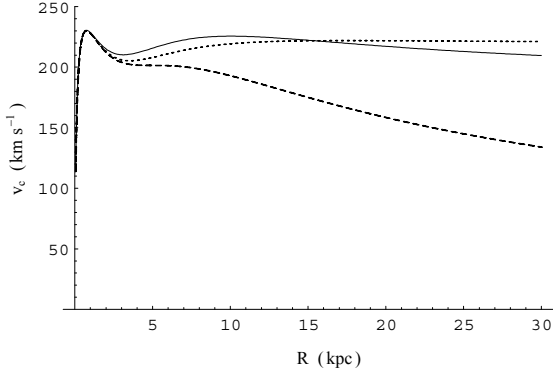


Figure 5. Rotation curve for the model of the Milky Way built with disc, bulge and halo (solid line). The dashed line shows the effect of removing the halo component, whilst the dotted line shows the sub-maximum model.

3 THE MIYAMOTO-NAGAI DISC MODEL

3.1 Preliminaries

The Miyamoto-Nagai (1975) disc has the following density distribution:

$$\rho(R, z) = B^2 M_d \frac{AR^2 + [A + 3\sqrt{B^2 + z^2}][A + \sqrt{B^2 + z^2}]^2}{4\pi[R^2 + (A + \sqrt{B^2 + z^2})^2]^{5/2}[B^2 + z^2]^{3/2}}. \quad (10)$$

Here, R and z are cylindrical coordinates. The $A \rightarrow 0$ and $B \rightarrow 0$ limits are

$$\rho(R, z) = \frac{3B^2 M_d}{4\pi} \frac{1}{(R^2 + z^2 + B^2)^{5/2}}, \quad (11)$$

$$\rho(R, z) = \frac{AM_d}{2\pi} \frac{1}{(R^2 + A^2)^{3/2}} \delta(z), \quad (12)$$

which are the Plummer (1911) model and the Kuzmin (1956) disc. The lensing properties of the former are discussed in Werner & Evans (2006) and the latter in Keeton & Kochanek (1998).

The Newtonian potential of the Miyamoto-Nagai disc is

$$\Phi(R, z) = -GM \left[R^2 + \left(A + \sqrt{z^2 + B^2} \right)^2 \right]^{-1/2}, \quad (13)$$

which is obtained from that of a point mass by the substitution

$$\hat{r}^2 \equiv R^2 + z^2 \longrightarrow R^2 + \left(A + \sqrt{z^2 + B^2} \right)^2. \quad (14)$$

3.2 The Projected Matter Density

The integral of the Newtonian potential along the line of sight (which is proportional to the deflection potential) and the integral of the 3-D density along the line of sight (which is the surface mass density relevant to lensing) are not generally analytic. However, in the most important case when the disc is viewed edge-on, these integrals are analytic. From

$$\Sigma(x', z') = \int_{-\infty}^{+\infty} \rho(x', y', z') y' \quad (15)$$

we obtain the dimensionless surface mass density

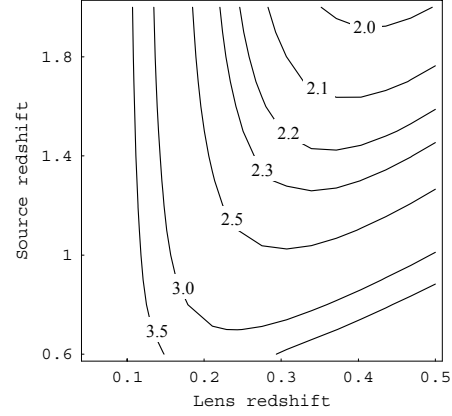


Figure 6. Dependence of σ_{cr} on lens and source redshifts in an Einstein-de Sitter universe. Contours are in units $10^9 M_{\odot} \text{ kpc}^{-2}$.

$$\kappa = \frac{b^2 m_d [2\sqrt{b^2 + y^2}(2a^2 + b^2 + y^2) + a(a^2 + 5b^2 + x^2 + 5y^2)]}{2(b^2 + y^2)^{3/2} [a^2 + b^2 + x^2 + y^2 + 2a\sqrt{b^2 + y^2}]^2}. \quad (16)$$

where we have set

$$x = \frac{x'}{\xi_0}, \quad y = \frac{z'}{\xi_0}, \quad m_d = \frac{M_d}{\pi \sigma_{\text{cr}} \xi_0^2},$$

$$a = \frac{A}{\xi_0}, \quad b = \frac{B}{\xi_0}, \quad (17)$$

so that (x, y) are dimensionless Cartesian coordinates in the lens plane.

Some level curves of $\log \kappa$ are shown in Figure 2. The model is useful, as the surface density distribution can be highly flattened. We see that a controls the overall extent of x - y asymmetry of the surface mass density ($a = 0$ is circularly symmetric), while b controls the sharpness of the ridge along the x -axis. Asymptotically, κ falls off along the x - and y -axes as

$$\kappa(x, 0) = \frac{m_d a}{2b} x^{-2} + O(x^{-4}), \quad (18a)$$

$$\kappa(0, y) = b^2 m_d y^{-4} + O(y^{-5}). \quad (18b)$$

Near the centre, the level curves of κ are ellipses with semiaxes $|a_{20}|$ and $|a_{02}|$, where

$$a_{20} = -m_d \frac{a + 4b}{2b(a + b)^4}, \quad \text{and} \quad (19a)$$

$$a_{02} = -m_d \frac{3a^2 + 9ab + 8b^2}{4b^3(a + b)^3} \quad (19b)$$

are coefficients in the Taylor expansion about the origin

$$\kappa(x, y) = \kappa(0, 0) + a_{20}x^2 + a_{02}y^2 + O(x^4, y^4, x^2y^2). \quad (20)$$

The isodensity contours (or isophotes given a constant mass-to-light ratio) of the model near the origin are the ellipses given by (19) and (20). The central ellipticity is

$$\epsilon_0 = 1 - \sqrt{\frac{a_{20}}{a_{02}}} = 1 - \sqrt{\frac{2(c + 4)}{(c + 1)(3c^2 + 9c + 8)}} \quad (21)$$

where $c \equiv a/b$. This vanishes when $c = 0$, as it should. Contours of constant central ellipticity are straight lines in the (a, b) plane, as shown in Figure 3. Moving along a line of given central ellipticity ϵ_0 away from the origin takes us from models that are disc-like in the outer parts to models that are intrinsically rounder.

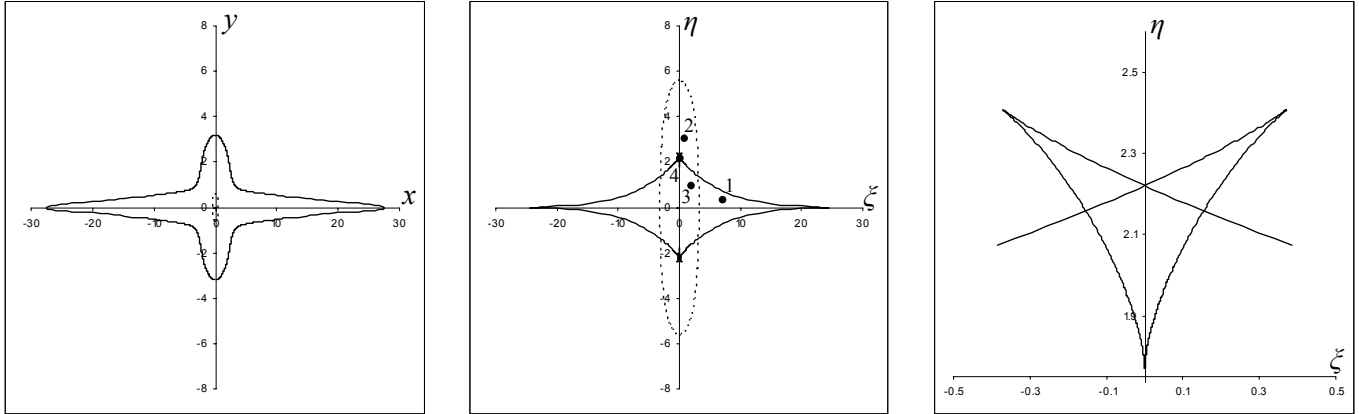


Figure 7. Critical curves (left panel) and caustics (centre panel) for lensing by a Milky Way galaxy. Note the small dotted critical curve around the origin. The right panel shows an enlargement of the upper butterfly cusps in the tangential or ‘astroid’ caustic. Dots in the source plane are source positions whose image configurations are shown in Figure 8.

3.3 Disc lensing

The deflection potential, related to the surface mass density by $\kappa(x, y) = \frac{1}{2} \nabla^2 \psi$, is

$$\psi = \frac{1}{2} m_d \log \left[x^2 + \left(a + \sqrt{y^2 + b^2} \right)^2 \right]. \quad (22)$$

Note that the $b \rightarrow 0$ limit is

$$\psi = \frac{1}{2} m_d \log \left[x^2 + (a + |y|)^2 \right], \quad (23)$$

not to be confused with the deflection potential of a point mass at $y = -a$, which is identical except $|y| \rightarrow y$. We remark that the very simple projected potential of the Miyamoto-Nagai disc seems not to have been noticed before. It is an attractive model for studies of lensing of arbitrarily flattened mass distributions.

The bending angle $\alpha = \nabla \psi$ is algebraic, with components

$$\alpha_x = \frac{m_d x}{x^2 + \left(a + \sqrt{y^2 + b^2} \right)^2},$$

$$\alpha_y = \frac{m_d y \left(a + \sqrt{y^2 + b^2} \right)}{\sqrt{y^2 + b^2} \left(x^2 + \left(a + \sqrt{y^2 + b^2} \right)^2 \right)}. \quad (24)$$

The critical curves and caustics can again be found numerically, solving

$$\det A \equiv (1 - \psi_{xx})(1 - \psi_{yy}) - (-\psi_{xy})^2 = 0 \quad (25)$$

by Newton-Raphson along radial lines. A sample showing qualitatively different configurations is shown in Figure 4, with the number of images for sources in different regions marked. In the upper panel ($\epsilon_0 = 0.16$), the tangential caustic is contained within the radial caustic. In the middle panel ($\epsilon_0 = 0.37$), the cusps of the tangential caustic are “naked”. The density contours become flatter still in the lower panel ($\epsilon_0 = 0.67$), and the tangential caustic has vanished. This is easily understood, as although the disc mass is the same, the central density diminishes on moving from the top to the bottom panels. Hence, this is the sequence from the two-lips to the single-lips caustic (see e.g., Kassiola & Kovner 1993).

Table 1. Mean magnifications and time delays (in days) for the core triplet, disc triplet and five image geometries for the Milky Way Model, the sub-maximum disc, and the Milky Way model with halo removed

	Milky Way	Sub-Maximum Disc	Halo Removed
5-image systems			
Total magnification	4.8	7.2	3.6
μ_5	2.5	3.6	1.9
μ_4	1.8	2.7	1.4
μ_3	0.37	0.72	0.30
μ_2	0.14	0.26	0.12
μ_1	0.005	0.007	0.006
$t_5 - t_1$	39.0	23.9	35.4
$t_4 - t_1$	31.6	18.8	29.1
$t_3 - t_1$	10.8	3.9	11.4
$t_2 - t_1$	8.5	3.0	8.7
Core triplets			
Total magnification	2.1	2.6	1.7
μ_3	1.6	2.0	1.2
μ_2	0.51	0.59	0.42
μ_1	0.02	0.02	0.02
$t_3 - t_1$	56.8	34.8	51.4
$t_2 - t_1$	51.3	31.5	46.6
Disc triplets			
Total magnification	4.2	6.2	3.4
μ_3	1.9	2.7	1.5
μ_2	1.6	2.3	1.3
μ_1	0.69	1.17	0.58
$t_3 - t_1$	1.27	0.30	1.54
$t_2 - t_1$	1.04	0.24	1.30

4 THE MILKY WAY AS A STRONG LENS

4.1 A Model for The Milky Way

A widely used model of the Milky Way is a combination of a Hernquist bulge, a Miyamoto-Nagai disc and a cored isothermal halo (see e.g., Paczyński 1990; Johnston et al. 1995; Dinescu et al. 1999). The Newtonian potential (up to an additive constant) is

$$\Phi = \Phi_b + \Phi_d + \Phi_h, \quad (26)$$

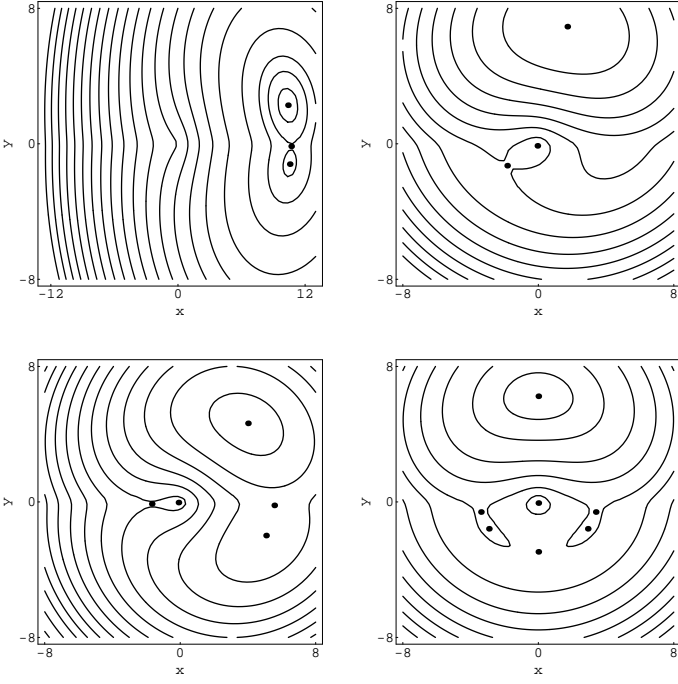


Figure 8. Fermat surfaces and image positions for the sources marked 1 to 4 in Figure 7. Top left: Source 1 produces a ‘disc’ three-image configuration, with two brighter images straddling a demagnified one in the plane of the disc. Top right: Source 2 produces a three-image geometry. The central image is highly demagnified. Bottom left: Five-image geometry from source 3. Again, the images in the plane of the disc are demagnified, with the central one highly demagnified. The images at (4,4.6) and (5,-2) have magnifications of about 1.7. Bottom right: Seven-image geometry of source 4, which is in a butterfly cusp. The highest magnification image is at (0, -2.9) with a magnification of about 7; the next highest are at ($\pm 2.9, -1.6$) with a magnification of about 5.6.

Table 2. Cross sections for the three, five and seven image geometries for the Milky Model, the sub-maximum disc, and the Milky Way model with halo removed

	Milky Way	Sub-Maximum Disc	Halo Removed
7 image	0.03	0.008	0.02
5 image	0.52	0.23	0.53
Total 3 image	1.57	1.03	1.61
Core triplet	0.89	0.85	0.82
Disc triplet	0.68	0.19	0.79

with Φ_b , Φ_d , and Φ_h the potentials of the bulge, disc and halo respectively:

$$\begin{aligned} \Phi_b &= \frac{-GM_b}{\hat{r} + r_0}, \\ \Phi_d &= \frac{-GM_d}{\sqrt{R^2 + (A + \sqrt{z^2 + B^2})^2}}, \\ \Phi_h &= \frac{GM_c}{r_c} \left[\frac{1}{2} \log\left(1 + \frac{\hat{r}^2}{r_c^2}\right) + \frac{r_c}{\hat{r}} \tan^{-1}\left(\frac{\hat{r}}{r_c}\right) \right]. \end{aligned} \quad (27)$$

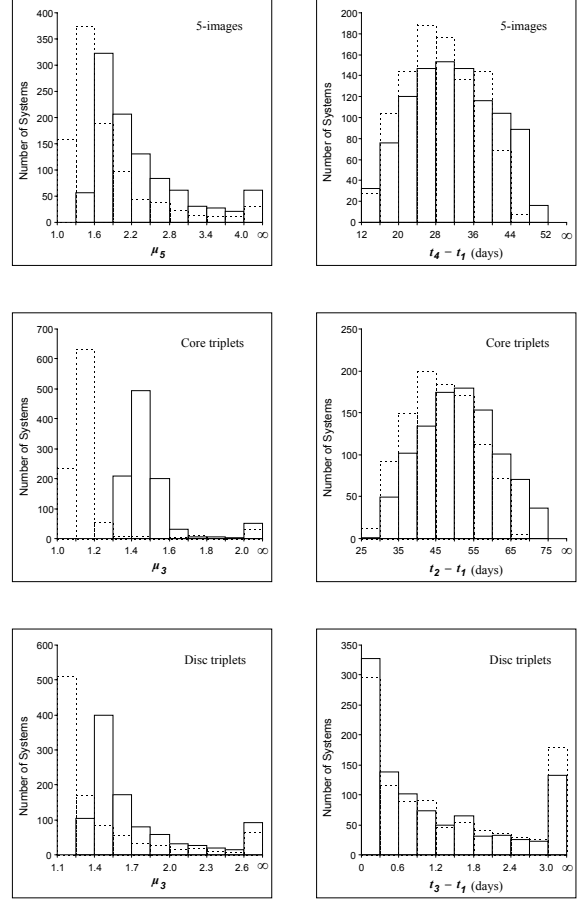


Figure 9. Histograms of the magnification of the brightest image (left column) and the maximum observable time delay between images (right column) for the five-image, core triplet and disc triplet configurations for the Milky Way model. The effect of removing the halo is indicated by the dotted histograms.

The halo potential corresponds to a cored isothermal sphere with density

$$\rho(\hat{r}) = \frac{\rho_c}{1 + \hat{r}^2/r_c^2} \quad (28)$$

where $M_c = 4\pi\rho_c r_c^3$. A typical set of values for the parameters are $M_b = 3.4 \times 10^{10} M_\odot$, $r_0 = 0.7$ kpc, $M_d = 10^{11} M_\odot$, $A = 6.5$ kpc, $B = 0.26$ kpc, $M_c = 5 \times 10^{10} M_\odot$, $r_c = 6.0$ kpc. The rotation curve of this model is shown in Figure 5. The local circular speed is ~ 220 km s $^{-1}$ and the model has a flattish rotation curve out to ~ 50 kpc.

Let us consider lensing by an edge-on galaxy with these components. (The effect of the disc component decreases rapidly as the inclination angle departs from zero). Choosing the scale $\xi_0 = r_0 = 0.7$ kpc, we readily obtain

$$a \approx 9.3, \quad b \approx 0.37, \quad \frac{m_d}{m_b} \approx 2.94. \quad (29)$$

As for the cored isothermal sphere, its dimensionless projected density $\kappa(r) = \sigma(r_0 r)/\sigma_{cr}$ is

$$\kappa(r) = \rho_h [1 + \lambda^2 r^2]^{-1/2}, \quad (30)$$

where the dimensionless ρ_h and λ are

$$\rho_h = \rho_c \frac{\pi r_c}{\sigma_{cr}}, \quad \lambda = \frac{r_0}{r_c}. \quad (31)$$

The bending angle is

$$\alpha_{\text{h}} = 2\rho_{\text{h}} \frac{r}{1 + \sqrt{1 + \lambda^2 r^2}}. \quad (32)$$

We include a halo for completeness, although we will show later that it has a small effect on the lensing properties of the model.

4.2 Typical Image Configurations

Consider, for concreteness, a galaxy like the Milky Way at a redshift of 0.4 lensing a quasar at a redshift of 1.5. In an Einstein-de Sitter universe with Hubble constant of $50 \text{ km s}^{-1} \text{ Mpc}^{-1}$, the redshift-distance relation gives $\sigma_{\text{cr}} \approx 2.17 \times 10^9 M_{\odot} \text{ kpc}^{-2}$, and the dimensionless mass/density parameters are $m_{\text{b}} \approx 10.2$, $m_{\text{d}} \approx 30$, $\rho_{\text{h}} \approx 0.16$. (Figure 6 shows the dependence of σ_{cr} on source and lens redshifts in an Einstein-de Sitter universe. As distances change, the dimensionless mass/density parameters scale accordingly). The critical curves and caustics of this lens are shown in Figure 7. There are 1, 3 or 5 images for sources in the different main regions. Notice that there is a tiny seven-image region within the butterfly cusp, shown enlarged in the rightmost panel. The formation of butterfly and swallowtail cusps in some lens models has been noted before – for example, in the study of disc-like and boxy ellipticals by Evans & Witt (2001), and in the study of the effects of halo substructure by Bradač et al. (2004). It is interesting that a straightforward disc and bulge system by itself can give rise to such higher order imaging, a result also found by Wang & Turner (1997).

For a fixed source position (ξ, η) , the images are at stationary points of the Fermat surface (see e.g. Schneider et al. (1992))

$$\phi_{(\xi, \eta)}(x, y) = \frac{1}{2}((x - \xi)^2 + (y - \eta)^2) - \psi(x, y), \quad (33)$$

where $\psi(x, y)$ is the deflection potential of the three-component (bulge, disc, halo) model:

$$\psi(x, y) = \psi_{\text{b}}(x, y) + \psi_{\text{d}}(x, y) + \psi_{\text{h}}(x, y), \quad (34)$$

and

$$\begin{aligned} \psi_{\text{b}} &= \frac{1}{2} m_{\text{b}} (\log \frac{r^2}{4} + 2\chi(r)), \\ \psi_{\text{d}} &= \frac{1}{2} m_{\text{d}} \log [x^2 + (a + \sqrt{b^2 + y^2})^2], \\ \psi_{\text{h}} &= 2\rho_{\text{h}} \lambda^{-2} [\sqrt{1 + \lambda^2 r^2} - \log(1 + \sqrt{1 + \lambda^2 r^2})]. \end{aligned} \quad (35)$$

Here, ψ_{b} and ψ_{h} are obtained from the relation

$$\psi_j(r) = 2 \int_0^r r' \kappa_j(r') \log\left(\frac{r}{r'}\right) dr'. \quad (36)$$

In Figure 8 are plotted Fermat surfaces for four characteristic source positions. The locations of the images are shown. The multiple-image configurations are different to those of spherical or elliptical lenses. In all four cases, images near the plane of the disc, typical of such lenses, are demagnified. The threefold image configurations may be split according to the whether the images are offset to one side of the galaxy centre ('disc triplets') or whether one image occurs close to the galaxy centre and the other two on either side ('core triplets'). In fivefold or sevenfold imaging, there is one central image whilst the remaining images lie on a broken Einstein ring.

4.3 Magnifications and Time Delays

Although interesting, the caustics are not directly observable. In addition to the positions of images, the observables of any strong lens may include the time delays and the ratios of image fluxes. The time delay is related to the Fermat potential via

$$\tau = \frac{\xi_0^2}{c} \frac{D_{\text{s}}}{D_1 D_{\text{ls}}} (1 + z_1) \phi_{(\xi, \eta)}(x, y) \quad (37)$$

where z_1 is the lens redshift, here taken by 0.4. To investigate the distributions of these quantities, we generate 10^3 source positions randomly within the caustics for each of the five-image and three-image cases and record the image properties. The magnifications are ordered μ_1, μ_2, \dots in increasing order. The means of the least highly magnified image, the second least highly magnified image, and so on, are recorded in Table 1, whilst histograms of the distributions are shown in Figure 9. Similarly, the time delays are ordered t_1, t_2, \dots in increasing order. For the 5 image and core triplet cases, the most delayed image is usually the unmagnified, highly demagnified central image, which corresponds to t_5 or t_3 respectively. The histograms show the maximum observable time delay, which is the largest time delay between the remaining images after the central image has been excluded.

Typically, the largest time delays occur for the core triplet configurations and next for the five-image systems. For lenses comparable to the Milky Way, it is of the order of month on average. However, the three images in disc triplets have very similar arrival times and so the time delays are much smaller, about a day on average. The images of highest magnification typically occur in five-image systems, for which the average total magnification is 4.7. Disc triplets are more highly magnified than core triplets, the average total magnifications being 4.2 and 2.1 respectively. Notice from Table 1 that disc triplets typically consist of two images of very similar brightness and one faint image. By contrast, the average magnifications of the three images of core triplets are more disparate.

5 ASTROPHYSICAL APPLICATIONS

In this section, we consider changes to our basic Milky Way model to investigate the lensing characteristics of sub-maximum discs (§5.1), the importance of the dark halo (§5.2) and the cross sections to multiple lensing (§5.3).

5.1 Spiral Galaxies and Maximum Discs

Here, we construct a spiral galaxy model with a sub-maximum disc. It has the same bulge as our Milky Way model, but the mass of the disc is halved. To maintain the amplitude of the rotation curve as $\sim 220 \text{ km s}^{-1}$ between 15 and 30 kpc, the core radius of the dark halo is adjusted to 4.5 kpc. In the sub-maximum model, the contributions of the disc, bulge and halo to the total circular speed 217 km s^{-1} at the Sun are 110, 123 and 141 km s^{-1} , respectively. In other words, the dark halo is now the single largest contributor to the rotational support at the Solar radius. The rotation curve of the model is shown in Fig. 5 as a dotted curve.

Given the caustics, numerical integration gives the areas of the various regions of multiple-imaging. It is traditional to normalize the cross sections with that of a singular isothermal sphere with circular velocity 220 km s^{-1} . This cross section is $\pi(\xi_{\text{sis}}/\xi_0)^2 r_0^2$, where (see e.g., Schneider et al. 1992)

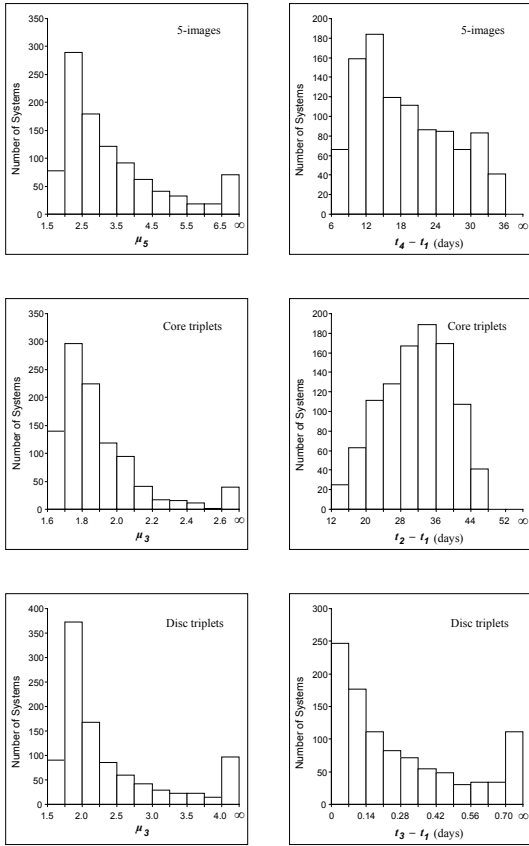


Figure 10. As Fig. 9, but for a sub-maximum disc spiral galaxy.

$$\xi_{\text{sis}} = \frac{\sigma_v^2}{\sigma_{\text{cr}} G}, \quad (38)$$

and the velocity dispersion is related to the circular velocity v_c by $v_c = \sqrt{2}\sigma_v$ (see e.g., Binney & Tremaine 1987). Just as in Keeton & Kochanek (1998), the magnification bias is neglected in the computation of the cross sections.

The cross sections for the multiple image geometries of the sub-maximum disc, normalized to that of an isothermal sphere, are given in Table 2. They can be directly compared to the same quantities for the Milky Way, which are also listed. For the sub-maximum disc, the cross section of disc triplet imaging decreases by a factor of $\sim 1/3$, five-imaging decreases by a factor of $\sim 1/2$, whilst the cross section of core triplets remains largely unchanged. This is because the astroid caustic shrinks dramatically in size, whilst the radial caustic undergoes a more modest change. In the absence of selection effects, a clear-cut difference between maximum and sub-maximum discs is that the former gives rise to core and disc triplets in roughly equal numbers, while the latter gives rise to mainly core triplets.

Table 1 shows the magnifications of all the image configurations, whilst Fig 10 gives histograms of maximum magnifications and time delays. Compared to the Milky Way, the total magnifications of all the image geometries has increased. This is because the size of the caustics has reduced, and so the source is typically close to a caustic when multiple imaging occurs. Although multiple imaging is less likely (the cross sections are smaller), the images are more highly magnified. Also, the time delays are smaller, as the total projected lensing mass is reduced.

Thus far, we have ignored the magnification bias. However, we

can roughly estimate its effect on the cross-sections using the mean magnifications listed in Table 1. Suppose, for example, the luminosity function of the sources has a slope of -2 . Then, the number of five image systems for the sub-maximum disc actually becomes similar to that for the Milky Way case. Similarly, the cross-sections of the core triplets and disc triplets in the sub-maximum case must be boosted by factors of ~ 1.5 and ~ 2.1 relative to the Milky Way case to incorporate the effects of magnification bias. Even so, core triplets will still predominate strongly over disc triplets.

5.2 The Role of the Dark Halo

Here, we take the Milky Way model and remove the dark halo. The resulting rotation curve is shown in Fig 5 as a dashed line. For the case of the Milky Way, the dark halo has an almost negligible effect on the size and shape of the caustics. The removal of the halo causes changes of $\sim 10\%$ in the cross sections of the disc and core triplets, as recorded in Table 2. However, the cross sections for total three-imaging (i.e., both core and disc) and five imaging are virtually unchanged. In fact, the cross section for multiple imaging is very slightly increased with the removal of the halo! This is because the astroid caustic increases in size slightly more than the radial caustic shrinks.

The effects of the dark halo on the image magnifications and the time delays are shown as the dotted histograms in Figure 9, whilst the averages are reported in Table 2. Although removal of the halo causes a slight diminution in the time delays, the shape of the time delay histograms are virtually unaffected. There are, however, some small but noticeable changes in the histograms of the magnifications. The total magnification diminishes by $\sim 30\%$ on removing the halo.

In our Milky Way model, the contributions of the disc, bulge and halo to the total circular speed 225 km s^{-1} at the Sun are $155, 123$ and 106 km s^{-1} , respectively. In other words, the dark halo makes a modest contribution to the rotation curve and hence the mass budget within the Solar circle. The typical scales probed by strong lensing are only of the order of a few kpc. Therefore, strong lensing by galaxies like the Milky Way does not probe the dark matter distribution in the halo very effectively. We conclude that a Hernquist bulge and Miyamoto-Nagai disc by themselves provide a realistic and analytically tractable lensing model for galaxies with maximum discs like the Milky Way.

5.3 Cross Sections for Multiple-imaging by Spiral Galaxies

Figures 11 and 12 show cross sections of multiple-imaging varying with the masses of disc and bulge, and with the shape parameters a and b of the two-dimensional disc model. The cross sections depend on the distances between lens, source and observer through σ_{cr} , but changing σ_{cr} simply corresponds to rescaling the dimensionless mass/density parameters m_b, m_d, ρ_h , so cross sections for $\sigma_{\text{cr}} \neq 2.17 \times 10^9 M_\odot \text{ kpc}^{-2}$ can also be read off from Figure 6, noting also that the singular isothermal sphere cross section, from (38), goes as σ_{cr}^{-2} . In all the panels, the position of the Milky Way galaxy is shown by a solid circle.

From Figure 11, we can read off the cross sections for a galaxy like the Milky Way (see also Table 2). The cross sections show that the core triplets, disc triplets and fivefold imaging are roughly equally likely. Seven imaging configurations are roughly a thousandfold times less likely. Increasing the mass of the bulge M_b at fixed disc mass M_d causes the cross section for disc triplets to diminish and that for core triplets to increase. Increasing the mass of

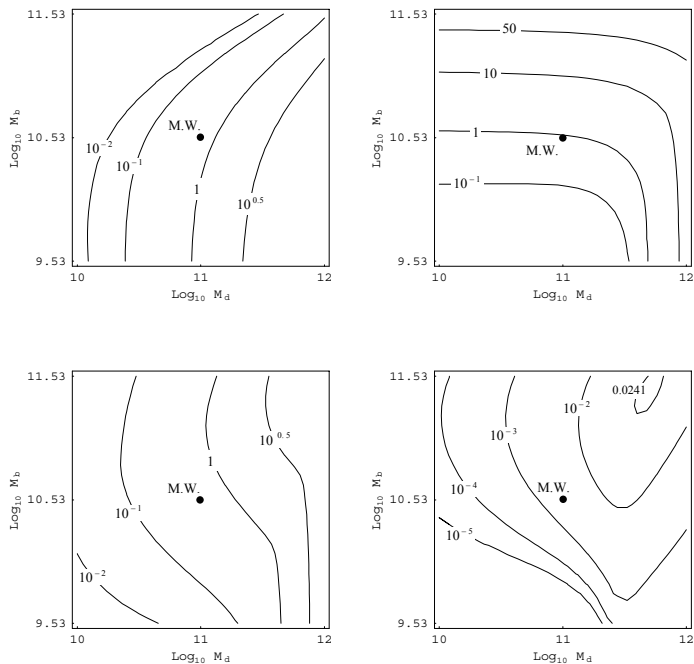


Figure 11. Multiple-imaging cross sections, as a fraction of the singular isothermal sphere cross section, varying with bulge and disc masses. Masses are in solar masses (the Milky Way values are in the centre of each plot). All other parameters are set to Milky Way values. Disc to bulge mass ratios are constant along diagonals. Top left: Disc triplet imaging cross section. Top right: Core triplet imaging cross section. Bottom left: Five-imaging cross section. Bottom right: Seven-imaging cross section. The butterfly cusp cannot be made arbitrarily large by making masses larger.

the disc M_d at fixed bulge mass M_b causes the cross sections for fivefold and sevenfold to increase.

To interpret Figure 12, we recall that the parameter a controls the ellipticity ($a = 0$ is circularly symmetric), while b controls the sharpness of the disc profile, $b \rightarrow 0$ corresponds to a razor thin disc). Increasing b at fixed a causes the cross sections of disc triplets and quintuplets to fall sharply, whilst leaving the cross section for core triplets largely unchanged.

6 CONCLUSIONS

We have analyzed the strong lensing properties of a realistic model of the Milky Way galaxy with a disc, bulge and halo, combined to produce a nearly flat rotation curve. All three components – the spherical Hernquist bulge, the Miyamoto-Nagai disc and the cored isothermal halo – have analytic deflection angles. There is strong evidence that the Milky Way galaxy possesses a maximum disc, in the sense that the contributions to the rotation curve by the disc and bulge at the Solar radius dominate over the contribution of the halo. The consequence of this is that the halo has a small effect on the strong lensing properties, including the magnifications and the time delays.

As a strong lens, the Milky Way galaxy exhibits four different kinds of multiple imaging geometries. They are (i) three images on one side of the galaxy centre (‘disc triplets’), (ii) three images with one close to the center (‘core triplets’), (iii) five images and (iv) seven images. For spiral galaxies, the lensing cross sections are dominated by edge-on models, as this is where the disc makes its

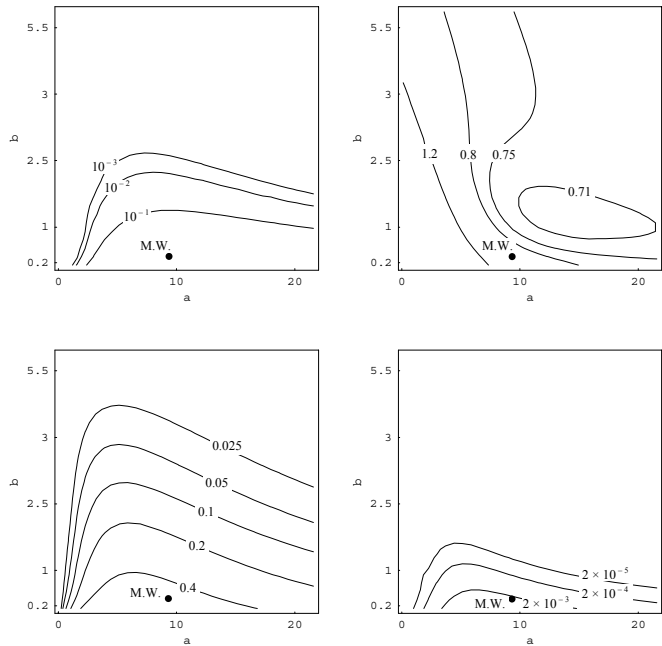


Figure 12. Multiple-imaging cross sections varying with the disc parameters a and b . All other parameters are set to Milky Way values. The four panels correspond to the same cross sections as in Figure 11.

presence known most effectively (Keeton & Kochanek 1998). The edge-on case is also the most important from the point of view of applications. In this instance, the cross sections show that the core imaging, disc imaging and fivefold imaging are roughly equally likely. The disc triplet cross section is also sensitive to the thickness of the disc and the mass of the bulge.

Disc triplets are a characteristic of gravitational lensing by spiral galaxies with maximum discs. They occur when the astroid caustic pierces the radial caustic. They consist of three images straddling one side of the lensing galaxy. The two outermost images are usually of comparable magnification, whilst the intervening image is much fainter. All three images have very similar arrival times and so the time delays are small, less than a day on average for our representative model. For comparison, the largest time delay between the observable images in core triplet or fivefold imaging is of the order of month on average.

Spiral galaxy lenses are rare compared to early-type galaxy lenses. The importance of gravitational lensing by nearly edge-on spirals is that it directly probes the shape of the matter distribution and therefore can break the degeneracy between flat disc and round halo. Face-on spirals are ineffective in discrimination, as the projected matter distribution from the disc is round. Even though only a few examples of nearly edge-on spiral galaxy lenses are known, this has already provided some important results. For example, Maller et al. (2000) has concluded that the spiral lens of B1600+434 does not have a maximum disc from detailed modelling of the positions and flux ratios of the two visible images.

The lensing properties of spiral galaxies with sub-maximum discs differ from maximum discs. The astroid caustic shrinks significantly in size, whilst the radial caustic shrinks more modestly. Therefore, the cross section of disc triplets is substantially reduced, whilst the cross section of core triplets remains roughly unchanged. The overall effect is to reduce the cross section to threefold (disc and core triplets) imaging by $\sim 2/3$ and to fivefold imaging by

1/2. The total magnification of the configurations is on average increased, but the time delays are decreased.

If maximum discs are typical, the lensing cross sections suggest that core triplets predominate only slightly over disc triplets. However, if sub-maximum discs are typical, then core triplets are $\sim 9/2$ times more likely than disc triplets. In fact, except for APM08279+5255, no disc triplet configurations are known. One possible interpretation of this scarcity is that the Milky Way is atypical and that spiral galaxies are usually sub-maximum. This conclusion derives some support from the detailed modelling of Maller et al. (2000) in the case of B1600+434.

It is also interesting that sevenfold imaging can occur for disc galaxies (c.f. Wang & Turner 1997; Evans & Witt 2001), even if the cross section is lower by a factor $\sim 10^{-3}$ compared to the cross sections for threefold or fivefold imaging. Our cross sections do not incorporate the effects of magnification bias, which will boost the likelihood by a significant amount (Turner, Ostriker, & Gott 1984). Note that the existence of higher order cusps increases the magnification of the quintuple image configurations as well. This is because the total magnification of the 5 images is increased by the appearance of the butterfly cusps inside the 5 image caustic. This fact has been neglected in all calculations of the numbers of expected 3 or 5 lens systems in the literature.

ACKNOWLEDGEMENTS

EMS thanks the Commonwealth Scholarship Commission and the Cambridge Commonwealth Trust for the award of a Studentship. We are grateful to the anonymous referee for a number of helpful suggestions. This work was supported by the European Community's Sixth Framework Marie Curie Research Training Network Programme, Contract No. MRTN-CT-2004-505183 "ANGLES"

REFERENCES

- Bartelmann M., 2000, *A&A*, 357, 51
 Bartelmann, M., Loeb, A. 1998, *ApJ*, 503, 48
 Binney, J. J., Evans, N. W. 2001, *MNRAS*, 327, L27
 Binney J., Tremaine, S. 1987, *Galactic Dynamics*, Princeton University Press, Princeton
 Bradač M., Schneider P., Lombardi M., Steinmetz M., Koopmans L.V.E., Navarro J.F. 2004, *AA*, 423, 797
 Courteau, S., Rix, H.-W. 1999, *ApJ*, 513, 561
 Dinescu D.I., et al., 1999, *AJ*, 117, 1792
 Englmaier, P., Gerhard, O. 1999, *MNRAS*, 304, 512
 Evans N.W., Hunter C. 2002, *ApJ*, 575, 68
 Evans N.W., Wilkinson M.I. 1998, *MNRAS*, 296, 800
 Evans N.W., Witt, H.J. 2001, *MNRAS*, 327, 1260
 Fellhauer M., et al. 2006, *ApJ*, 651, 167
 Häfner, R., Evans, N. W., Dehnen, W., Binney, J. 2000, *MNRAS*, 314, 433
 Helmi A. 2004, *MNRAS*, 351, 643
 Hernquist L., 1990, *ApJ*, 356, 359
 Hunter C., Evans N. W., 2001, *ApJ*, 554, 1227
 Ibata R.A., Lewis G.F., Irwin M.J., Lehár J., Totten E.J. 1999, *AJ*, 118, 1922
 Jackson N. et al, 1998, *MNRAS*, 296, 483
 Jackson N., Xanthopoulos E., Browne I.W.A., 2000, *MNRAS*, 311, 389
 Johnston K.V. et al., 1995, *ApJ*, 451, 598
 Kassiola A., Kovner I., 1993, *ApJ*, 417, 450
 Kawano Y. et al., 2004, *PASJ*, 56, 253
 Keeton C.R., 2001, astro-ph/0102340
 Keeton C.R., Kochanek C.S., 1998, *ApJ*, 495, 157
 Koopmans L.V.E., de Bruyn A.G, Jackson N., 1998, *MNRAS*, 295, 534
 Kormann R., Schneider P., Bartelmann M., 1994, *A&A*, 284, 285
 Kuzmin G., 1956, *Astron. Zh.*, 33, 27
 Maller, A. H., Simard, L., Guhathakurta, P., Hjorth, J., Jaunsen, A. O., Flores, R. A., & Primack, J. R. 2000, *Apj*, 533, 194
 Miyamoto M., Nagai R., 1975, *PASJ*, 27, 533
 Möller O., Blain A.W., 1998, *MNRAS*, 299, 845
 Paczyński B., 1990, *ApJ*, 348, 485
 Palunas, P., & Williams, T. B. 2000, *AJ*, 120, 2884
 Plummer H.C., 1911, *MNRAS*, 71, 460
 Sackett, P. D. 1997, *ApJ*, 483, 103
 Schmidt R., Webster R.L., Geraint L.F., 1998, *MNRAS* 295, 488
 Schneider P., Ehlers J., Falco E.E., 1992, *Gravitational Lenses*, Springer-Verlag, New York
 Sellwood, J. A., Sanders, R. H. 1988, *MNRAS*, 233, 611
 Toomre A., 1963, *ApJ*, 138, 385
 Trott, C. M., Webster, R. L. 2002, *MNRAS*, 334, 621
 Turner E.L., Ostriker J.P., Gott J.R. 1984, *ApJ*, 284, 1
 Wang, Y., Turner, E. L. 1997, *MNRAS*, 292, 863
 Werner M., Evans N.W., 2006, *MNRAS*, 368, 1362
 Winn J.N., Hall P.B., Schlechter P.L., 2003, *ApJ*, 597, 672
 Witt H.J., 1996, *ApJ*, 472, L1
 Witt H.J., Mao S., 1997, *MNRAS*, 291, 211